

Experimental observation and spin texture of Dirac node arcs in tetradymite topological metals

J. Dai,^{1,*} E. Frantzeskakis,^{1,†} N. Aryal,^{2,3,‡} K.-W. Chen,^{2,3,§} F. Fortuna,¹ J. E. Rault,⁴ P. Le Fèvre,⁴ L. Balicas,^{2,3} K. Miyamoto,⁵ T. Okuda,⁵ E. Manousakis,^{2,3,6} R. E. Baumbach,^{2,3} and A. F. Santander-Syro^{1,¶}

¹ *Université Paris-Saclay, CNRS, Institut des Sciences Moléculaires d'Orsay, 91405, Orsay, France*

² *National High Magnetic Field Laboratory, Florida State University, United States of America*

³ *Department of Physics, Florida State University, United States of America*

⁴ *Synchrotron SOLEIL, L'Orme des Merisiers, Saint-Aubin-BP48, 91192 Gif-sur-Yvette, France*

⁵ *Hiroshima Synchrotron Radiation Center (HSRC), Hiroshima University,*

2-313 Kagamiyama, Higashi-Hiroshima 739-0046, Japan

⁶ *Department of Physics, National and Kapodistrian University of Athens,*

Panepistimioupolis, Zografos, 157 84 Athens, Greece

(Dated: May 18, 2021)

We report the observation of a non-trivial spin texture in Dirac node arcs, novel topological objects formed when Dirac cones of massless particles extend along an open one-dimensional line in momentum space. We find that such states are present in all the compounds of the tetradymite M_2Te_2X family ($M=Ti, Zr$ or Hf and $X=P$ or As), regardless of the weak or strong character of the topological invariant. The Dirac node arcs in tetradymites are thus the simplest possible, textbook example, of a type-I Dirac system with a single spin-polarized node arc.

During the last decade various topological phases of matter such as the quantum spin Hall effect [1, 2], topological insulators [3, 4], topological superconductors [5], topological crystalline insulators [6], or Dirac and Weyl semimetals [7–10], have provoked an immense interest of the scientific community. Scientific excitement in topological matter stems from its high potential in novel applications such as building blocks of quantum information in the form of Majorana zero modes [11, 12], spin generators in spintronic circuits [13, 14] and optoelectronic nanodevices [15].

Dirac cones, the simplest form of topological states, can have variable dimensionality in momentum space ranging from 1D to 3D, and display different topological characteristics giving rise to weak and strong topological states. Moreover, when the Dirac cone extends along an open 1D line in momentum space, the series of adjacent Dirac points form so-called “Dirac node arcs” [16, 17]. Each variation in dimensionality, topological characteristics and k -space fingerprint of the Dirac point (i.e. a single node vs. a 1D line or arc) defines a new class of topological matter: quantum spin Hall insulators for 1D states [2, 18], strong or weak topological insulators for 2D states [19–21], Dirac and Weyl semimetals for 3D states [8–10, 22], nodal-line semimetals for Dirac nodal lines [23–25].

There is however a new family of topological metals that is predicted to combine many of the above special features. This is the tetradymite family M_2Te_2X (with $M=Ti, Zr$ or Hf and $X=P$ or As), in which both strong and weak topological surface states have been theoretically predicted [26–29], interestingly accompanied by Dirac node arcs in one of its members [29]. In this work, we employ angle- and spin-resolved photoemission spectroscopy (ARPES and SARPES) to experimentally

demonstrate the crucial -yet missing- element that such Dirac node arcs are *spin-polarized*, showing a non-trivial spin-texture, and hence they meet all the essential requirement to be classified as *topological Dirac node arcs*. Moreover, our results prove that *all* compounds of the family share the exotic feature of a Dirac node arc. Compared to Dirac node arcs observed in topological line-node semimetals [17, 30], or to multiple node-arcs in type-I Dirac systems [16], the unique Dirac node arc in the tetradymite M_2Te_2X compounds is thus the simplest possible, textbook example, of a type-I Dirac system with a single spin-polarized node arc.

ARPES experiments were performed at the CASIOPEE beamline of Synchrotron SOLEIL (France), and Spin-ARPES experiments were performed using the ESPRESSO machine at beamline 9B of the Hiroshima Synchrotron Radiation Center (HiSOR, Japan) [31]. Typical energy and angular resolutions were 15 meV and 0.25° . The single crystals of M_2Te_2X ($M=Ti, Zr$ or Hf and $X=P$ or As) [26] were cleaved *in situ* at temperatures below 25 K and pressure in the range of 10^{-11} mbar, and were kept at those conditions during the measurements. The Supplementary Material provides complete technical details about the sample growth, crystal structure, ARPES and Spin-ARPES measurements

Figure 1(a) presents the experimental constant energy contours of Ti_2Te_2P at various binding energies. The Fermi surface consists of six petal-like electron pockets centered at the \bar{M} points of the surface Brillouin zone and a weaker hexagonal contour in the immediate vicinity of $\bar{\Gamma}$ [28], shown in the inset. The smallest point-like contour at $\bar{\Gamma}$ is residual intensity coming from a hole-like band whose maximum lies just below E_F for Ti_2Te_2P [28]. As the binding energy increases, the petal-like contours evolve into linear features along the $\bar{\Gamma M}$ high symmetry

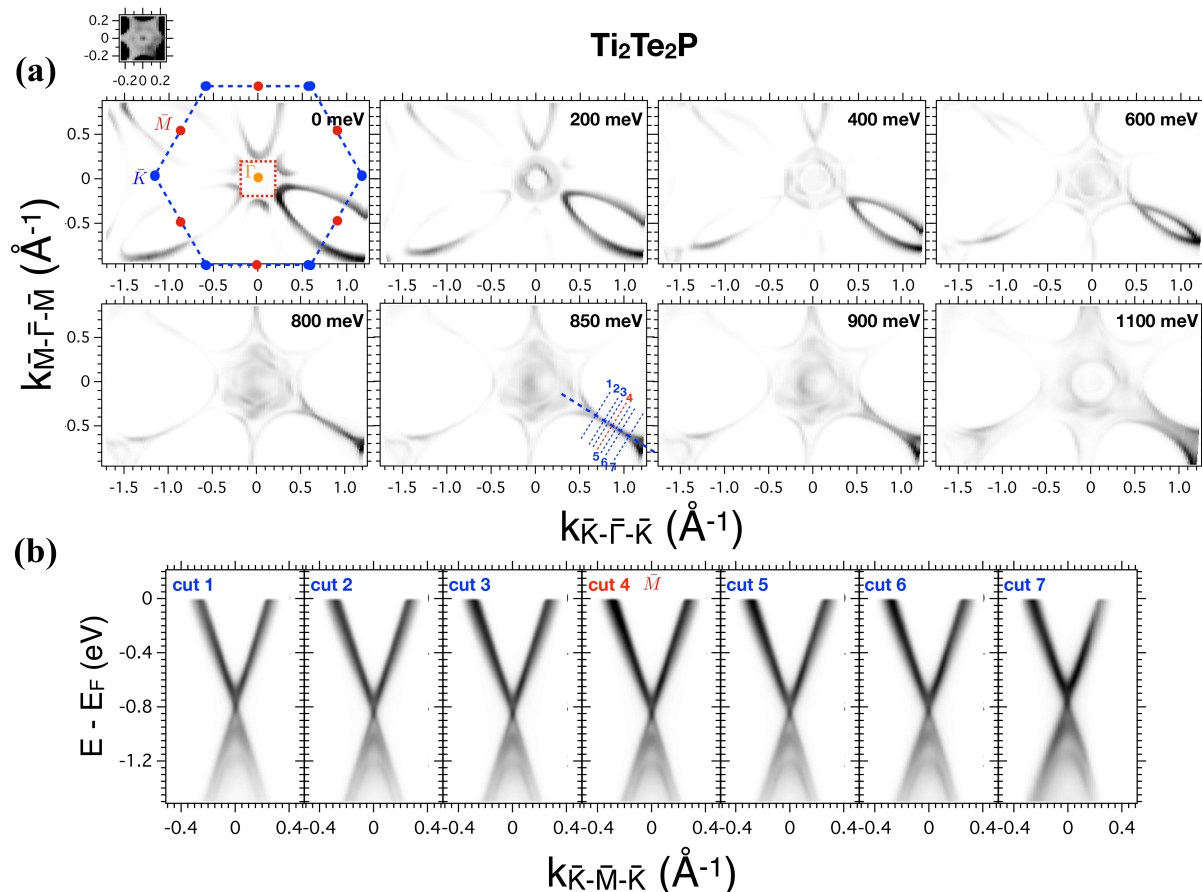


Figure 1. (Color online) (a) Constant energy maps at various binding energies. A linear feature appears at an approximate binding energy of 850 meV. The dashed blue hexagon marks the borders of the surface-projected Brillouin zone. The dashed red square indicates the area with saturated contrast shown in the inset above the top left panel. (b) Energy-momentum dispersion showing a persistent Dirac-like dispersion along various k -paths marked by dashed lines in (a). All data were collected using photons of 50 eV and linear horizontal polarization. The temperature was 6 K.

lines. The energy-momentum dispersion along $\bar{K}\bar{M}\bar{K}$ reveals a Dirac cone that is typical for all compounds of the tetradymite family $\text{M}_2\text{Te}_2\text{X}$. Our previous first-principles calculations [28] revealed the non-trivial origin of such Dirac-like state. The binding energy of the Dirac point for $\text{Ti}_2\text{Te}_2\text{P}$ is 0.85 eV, that is 200-300 meV lower than for other compounds of this family (see Fig. 5). Interestingly, as shown in panel (b) by the energy-momentum maps along k -paths parallel to $\bar{K}\bar{M}\bar{K}$, this Dirac-like dispersion is present all along the linear features of the constant energy map, with the Dirac point shifting to slightly lower binding energies as one moves away from \bar{M} (see Fig. 6). These results are in agreement with a previous study on $\text{Hf}_2\text{Te}_2\text{P}$ [29], and they present a first indication that these linear features may correspond to topologically non-trivial Dirac node arcs. The Supplementary Material presents additional data and analyses for the linearly dispersing Dirac states in the vicinity of \bar{M} along $\bar{K}\bar{M}\bar{K}$, as well as for the Dirac node arcs, for $\text{Hf}_2\text{Te}_2\text{P}$, $\text{Zr}_2\text{Te}_2\text{P}$, $\text{Ti}_2\text{Te}_2\text{P}$ and $\text{Zr}_2\text{Te}_2\text{As}$.

Without any information on their spin texture, the lin-

ear features in the constant energy maps of the $\text{M}_2\text{Te}_2\text{X}$ compounds (see Fig. 6), even if associated to a cone-like dispersion, cannot be unambiguously assigned to topologically non-trivial Dirac node arcs. Thus, a direct measurement of their spin polarization is necessary to elucidate if they correspond to non-trivial states. As we will see next, our SARPES data on $\text{Ti}_2\text{Te}_2\text{P}$ and $\text{Hf}_2\text{Te}_2\text{P}$ reveal an appreciable spin polarization of the Dirac cones both along $\bar{K}\bar{M}\bar{K}$ and at parallel k -paths. As a result, they establish the linear features of the constant energy maps as topologically non-trivial 1D Dirac node arcs.

Figure 2 presents spin-integrated and spin-resolved ARPES results acquired using the ESPRESSO setup at HiSOR [31] on $\text{Ti}_2\text{Te}_2\text{P}$, Figs. 2(a, b), and $\text{Hf}_2\text{Te}_2\text{P}$, Figs. 2(c, d, e). The spin-integrated ARPES results on both compounds, panels (a, b, d), reproduce the main experimental features discussed before. Our goal is to establish the spin texture of the Dirac-like dispersion along $\bar{K}\bar{M}\bar{K}$ by measuring its in-plane spin component along the orthogonal $\bar{\Gamma}\bar{M}$ direction. In the case of $\text{Ti}_2\text{Te}_2\text{P}$, the energy-dependent spin polarization has been acquired at

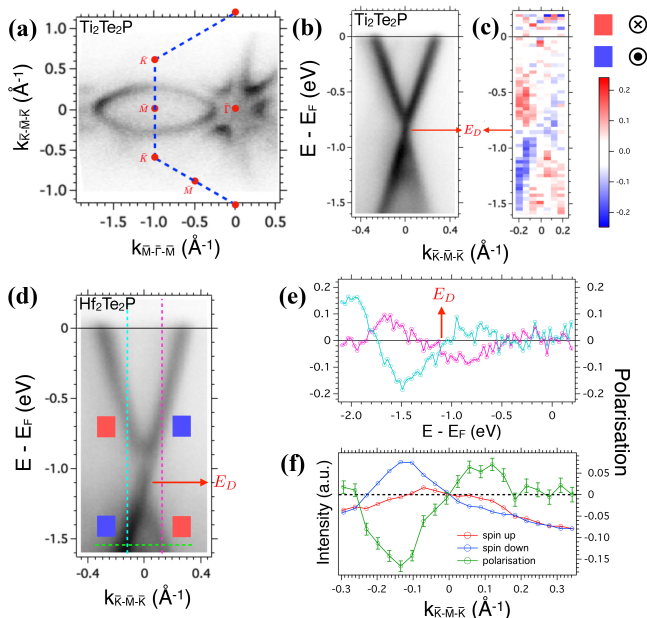


Figure 2. (Color online) (a) In-plane Fermi surface map of $\text{Ti}_2\text{Te}_2\text{P}$ showing a sixfold symmetry. (b, c) Near- E_F band structure of $\text{Ti}_2\text{Te}_2\text{P}$ along the $\overline{\text{KMK}}$ high-symmetry line with spin-integrated (b) and spin-resolved (c) ARPES, showing a Dirac-like dispersion with clear spin polarization. The color scale in (c) represents the sign and value of the in-plane spin polarization along $\overline{\Gamma\text{M}}$ with blue (red) pointing towards to (away from) the reader. (d) Near- E_F band structure of $\text{Hf}_2\text{Te}_2\text{P}$ along the $\overline{\text{KMK}}$ high-symmetry line. Blue (red) squares indicate branches of the Dirac cone with spin polarisation pointing towards to (away from) the reader. (e) Energy dependent spin polarization of $\text{Hf}_2\text{Te}_2\text{P}$ at the constant momenta indicated by the vertical light blue and magenta dashed lines in (c). (f) Spin-resolved momentum distribution curves (blue, red) and momentum dependent spin polarization (green) at the constant energy indicated by the horizontal green dashed line in (d). Spin up/down means parallel/anti-parallel to $\overline{\Gamma\text{M}}$. The Dirac point at energy E_D is shown by a red arrow in panels (b-e). All data were collected with LH polarized photons of 55 eV. The temperature was 25 K.

different k -locations of the Dirac cone by measuring the spin-resolved energy distribution curves or EDCs (see the Supplementary Material). Panel (c) is a stack of the energy-dependent polarization curves where the color scale represents the sign of the in-plane spin polarization with blue (red) pointing towards to (away from) the reader. The Dirac-like dispersion is reproduced with a clear polarization reversal between the left and right sides of the cone. Moreover, our data reveal another reversal of the in-plane spin polarization between the top and bottom parts of the cone, in good agreement with results on Bi-based topological insulators [32].

Similar conclusions can be drawn on the in-plane spin polarization of $\text{Hf}_2\text{Te}_2\text{P}$, whose spin-integrated Dirac cone is shown in panel (d). The energy dependent spin polarization at both sides of the Dirac cone, shown in panel (e), has been acquired by means of spin-resolved EDCs. The polarization of each curve reverses above

and below the Dirac point, while the two curves have opposite polarizations at a given binding energy. As expected, at the binding energy of the Dirac point (1.1 eV), the spin polarization is vanishingly small. Consistent information can be obtained with spin-resolved momentum distribution curves (MDCs), shown in panel (f). Here the change in the direction of the in-plane spin polarization component is tracked as a function of momentum at a fixed binding energy at the bottom part of the Dirac cone (1.55 eV). At this binding energy, the polarization changes from negative to positive as one passes from the left to the right branch of the Dirac cone. This is in perfect agreement with the data shown in panel (e) where the light blue (magenta) curve obtained at the left (right) side of the cone shows a negative (positive) polarization at a binding energy of 1.55 eV. Based on the results presented in Fig. 2, we can experimentally confirm that the Dirac cone in compounds of the tetradymite family $\text{M}_2\text{Te}_2\text{X}$ is spin polarized.

Having established the spin polarization of the Dirac cone at $\overline{\text{M}}$, we now turn our attention to the characteristics and the spin texture of the linear features observed in the constant energy maps of Fig. 1. Figs. 3(a) and 3(b) show once more how the petal contours of the Fermi surface of $\text{Ti}_2\text{Te}_2\text{P}$ evolve into linear features at the binding energy of the Dirac point. Panel (c) presents another measurement of the constant energy contours at the Dirac point energy, acquired with the experimental setup at HiSOR right before spin-resolved measurements. Figures 3(d-f) present the spin-resolved EDCs and the resulting energy-dependent spin polarization acquired at the left side of the Dirac cones, panels (g-i), themselves observed along three different k -paths parallel to $\overline{\text{KMK}}$: cuts (1) - (3) in panel (c). These data show that an in-plane spin-polarization exists not only along the $\overline{\text{KMK}}$ high-symmetry direction but also all along the Dirac node arc. We conclude that the Dirac cones along $\overline{\text{KFK}}$ not only share a common energy for their Dirac point, forming the node arc, but also that they exhibit an identical spin polarization. Our experimental results can therefore establish that the observed linear features at the Dirac point energy correspond indeed to topologically non-trivial Dirac node arcs.

The aforementioned results confirm the presence of spin polarized electrons with a Dirac-like dispersion in one direction and a very large effective mass in the perpendicular direction (see also Fig. 6, Supplementary Material). Such qualitatively different behaviors may stem from the mixed contributions of p ($\approx 60\text{-}70\%$) and d ($\approx 20\text{-}30\%$) orbital states to the topological surface state at $\overline{\text{M}}$ (see Figs. 8 and 9, Supplementary Material), as suggested for Ru_2Sn_3 [33]. Provided that the Dirac cone could be tuned near E_F , compounds of this family could give rise to highly anisotropic 2D electron systems with spin polarized carriers. Our results prove that the existence of the Dirac node arcs is an inherent property of

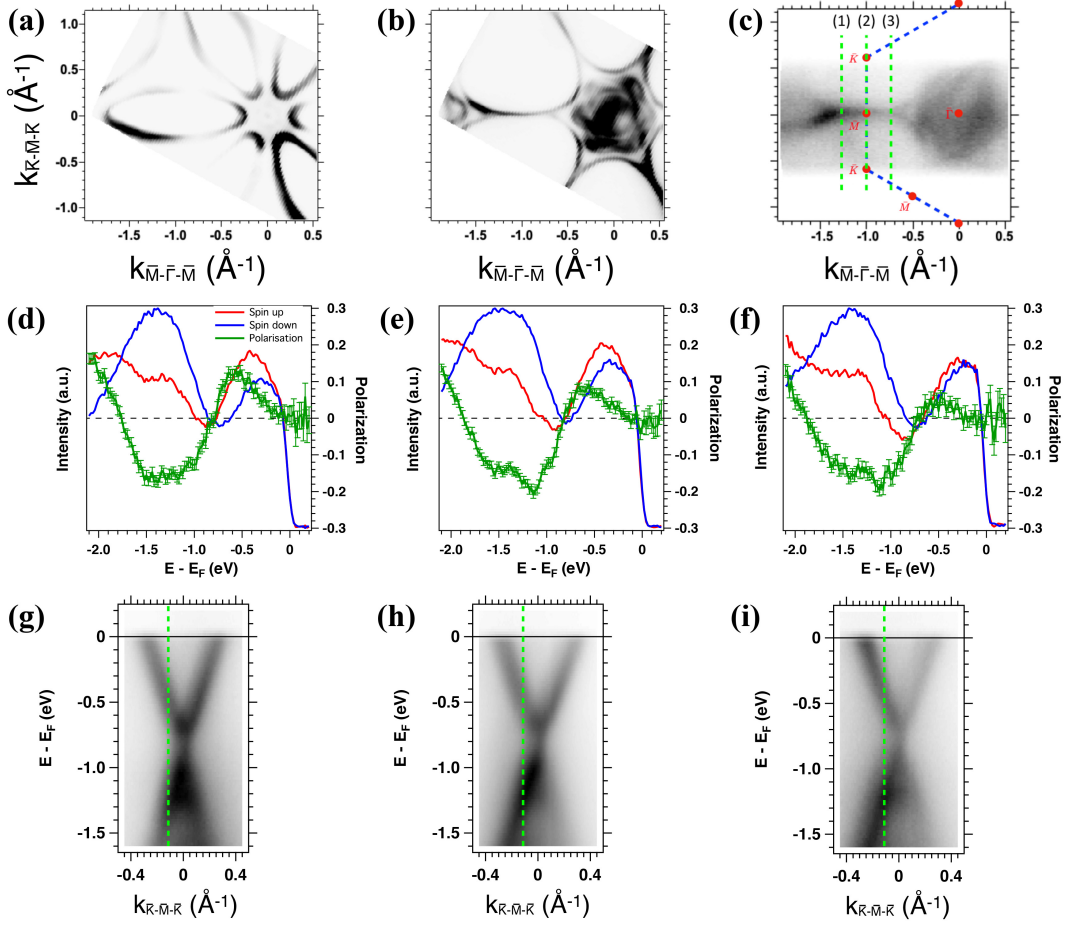


Figure 3. (Color online) (a), (b) Spin-integrated ARPES results obtained at synchrotron SOLEIL with LH polarized photons of 50 eV at a temperature of 6 K showing the Fermi surface contours of $\text{Ti}_2\text{Te}_2\text{P}$ (a) and the existence of linear features at a binding energy of 0.85 eV (b). (c) Same as panel (b) but measured with LH photons of 55 eV at the ESPRESSO spin-resolved ARPES setup of beamline 9B at HiSOR. Path (1) corresponds to data shown in panels (d) and (g), path (2) to panels (e) and (f), and path (3) to panels (f) and (i). (d)-(f) Spin-resolved EDCs (red, blue) and energy dependent in-plane spin polarization parallel to $\bar{\Gamma}\bar{M}$ (green) measured at the left branch of the Dirac cones [panels (g)-(i)], themselves obtained at different k -locations along the Dirac node arc. (g)-(i) Energy-momentum dispersion along the k -paths indicated in panel (c), with overlaid vertical dashed lines showing the k -location of the spin-resolved EDCs shown in panels (d)-(f). Panels (c)-(f) were all measured with LH photons of 55 eV at a temperature of 25 K.

all studied $\text{M}_2\text{Te}_2\text{X}$ compounds, regardless of their topological character at \bar{M} , rather than being related to the weak topological character and the weak interlayer coupling of $\text{Hf}_2\text{Te}_2\text{P}$ as suggested in Ref. 29. After all, the Dirac states at \bar{M} have a strong topological character for $\text{Zr}_2\text{Te}_2\text{P}$, $\text{Zr}_2\text{Te}_2\text{As}$ and $\text{Ti}_2\text{Te}_2\text{P}$ [27, 28].

The experimental observation of an in-plane spin polarization of the Dirac node arcs in a direction normal to the arcs' crystal momentum (i.e., parallel to $\bar{\Gamma}\bar{M}$) agrees with the main direction of the spin polarized vector in topological insulators and Rashba compounds [32, 34]. The Supplementary Material shows additional data for the out-of-plane spin polarization, and discusses the magnitude of the observed spin polarization.

Surprisingly, there is substantial spin polarization at energies $E - E_F < -1.5$ eV, i.e. below the lower branch of the Dirac cone (Figs. 2 and 3). This observation has been

reproduced in different experimental runs for all cleaved surfaces of both compounds studied here ($\text{Hf}_2\text{Te}_2\text{P}$ and $\text{Ti}_2\text{Te}_2\text{P}$). On the other hand, it is not observed for compounds that do not belong to the $\text{M}_2\text{Te}_2\text{X}$ that were studied with the same setup. Therefore, we believe that it is not due to an experimental artifact and it may indeed reveal the existence of spin polarized states at larger binding energies. This scenario is in agreement with the experimental observation (e.g. Fig. 1) and the theoretical prediction [28] of hole-like surface states at the same energy range. A possible explanation is the spin-polarized surface-confined states due to the Rashba-Bychkov effect, which have been repeatedly observed in the band structure of Bi_2Se_3 , in the vicinity of both the upper and the lower branches of its Dirac cone [35, 36].

In conclusion, by means of spin-integrated and spin-resolved ARPES, we unambiguously proved the existence

of type-I *topological* Dirac node arcs in compounds of the M_2Te_2X family. Our data showed bands with linear dispersion in one direction and a very large effective mass in the perpendicular direction. Our direct measurement of their spin polarization vector shows substantial in-plane spin polarization in the direction perpendicular to the crystal momentum of the Dirac node arcs, all along the linear features in the constant energy contours. This helical arrangement of the electron spins is opposite for the upper and lower branches of the Dirac cone forming the arc. Taken together, these observations establish the existence of topological Dirac node arcs in all studied compounds of the M_2Te_2X family regardless of their different topological characters. An exciting perspective for future research would be to tune, by doping or pressure, the energy of the Dirac points in the M_2Te_2X family to the Fermi level.

We thank F. Bertran for assistance during ARPES measurements at CASSIOPEE (Synchrotron SOLEIL). ARPES work at ISMO was supported by public grants from the French National Research Agency (ANR), project Fermi-NES_t No ANR-16-CE92-0018. Experiments at HiSOR were performed under the approval of the Program Advisory Committee (proposals 16BG014 and 17BU010). R.B. acknowledges support from the National Science Foundation through NSF/DMR1904361. L.B. is supported by DOE-BES through award DE-SC0002613.

SUPPLEMENTARY MATERIAL

Crystal structure

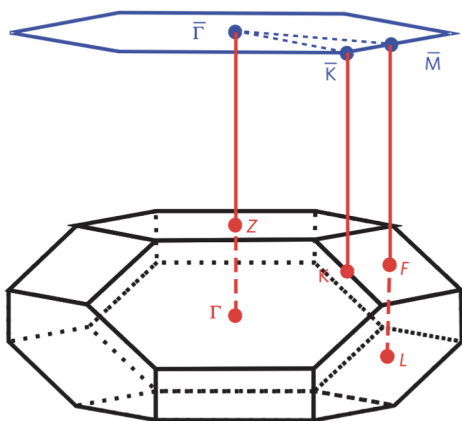


Figure 4. The rhombohedral Brillouin zone projects onto a hexagonal surface Brillouin zone. The time-reversal invariant momentum (TRIM) points Γ , Z , F , L are labeled as red dots.

The crystal structure of M_2Te_2X (with $M = \text{Ti, Zr or}$

Hf , and $X = \text{P or As}$) has the symmetry of the rhombohedral space group $R\bar{3}m$ (No. 166). The corresponding bulk Brillouin zone (rhombohedral) and the reduced surface Brillouin zone (hexagonal) are shown in Fig. 4. The bulk TRIM points (Γ , Z , and 3 pairs of F and L) are labeled as red dots. Depending on the calculated parities, the topological surface states might be observed at $\bar{\Gamma}$ and/or \bar{M} that correspond to the surface projection of the aforementioned bulk TRIM points.

Methods

Single crystal growth. Single crystals of M_2Te_2X ($M=\text{Ti, Zr or Hf}$ and $X=\text{P or As}$) were grown using the chemical vapor transport method that was described elsewhere [26]. The precursor material consisted of stoichiometric polycrystals themselves prepared by the reaction of raw elements at 1000°C for 24 hours. The resulting powders were sealed under vacuum with 3 mg/cm^3 of iodine in quartz tubes. The tubes were subsequently placed in a resistive tube furnace with a temperature gradient with 800°C (source) and 900°C (drain) for 21 days. Exfoliable single crystal specimens formed in the cold zone of the ampoule, having a hexagonal plate shape and the crystallographic c -axis oriented perpendicular to the plate face. Single crystals were cleaved in UHV conditions to expose an adsorbate-free surface right before the ARPES experiments.

Spin-integrated ARPES. ARPES experiments were performed at the CASSIOPEE beamline of Synchrotron SOLEIL and at beamline 9B of the Hiroshima Synchrotron Radiation Center (HiSOR) using hemispherical electron analyzers with vertical and horizontal slits, respectively. Typical energy and angular resolutions were 15 meV and 0.25° . The polarization of incoming photons was linear horizontal. Measurements were performed at 6 K (SOLEIL) or 25 K (HiSOR), under a typical pressure in the range of 10^{-11} mbar .

Spin-resolved ARPES. Spin-ARPES experiments were performed using the ESPRESSO machine at beamline 9B of the Hiroshima Synchrotron Radiation Center (HiSOR) [31]. Spin separation of the emitted photoelectrons is achieved by means of very low energy diffraction (VLEED) detectors. In the VLEED detector, photoelectrons are scattered by a $\text{Fe}(001)\text{-p}(1\times 1)\text{-O}$ film grown on a $\text{MgO}(001)$ substrate [37]. The FeO film is magnetized by a pair of solenoids that impose two orthogonal magnetization axes in its surface. In order to measure the component of the spin normal to the Dirac node arc (parallel to the $\bar{\Gamma}\bar{M}$ line intersecting the arc), the sample was aligned with the magnetization axis of the FeO film. A second VLEED detector oriented at 90° with respect to the first one allows for measurements of all three spin

polarization components. The spin asymmetry (A) of the electron beam is measured by switching the magnetization of the of FeO film and it is given by:

$$A = \frac{I_A - I_B}{I_A + I_B}$$

where I_A and I_B are the intensities measured using opposite magnetizations of the FeO film. The spin polarization P is related to the spin asymmetry of the scattered electrons:

$$P = \frac{A}{S} = \frac{I_{\uparrow} - I_{\downarrow}}{I_{\uparrow} + I_{\downarrow}}$$

where I_{\uparrow} and I_{\downarrow} are the spin populations of opposing spins where S denotes the Sherman function that was equal to 0.18 for the data shown in Fig. 2 of the main text, and 0.25 for the data shown in Fig. 3 of the main text and Fig. 7. Finally, the spin populations I_{\uparrow} and I_{\downarrow} can be written as [38]:

$$I_{\uparrow} = (1 + P) \frac{I_A + I_B}{2} \quad \text{and} \quad I_{\downarrow} = (1 - P) \frac{I_A + I_B}{2}$$

The energy (or momentum) dependence of I_{\uparrow} and I_{\downarrow} yield the spin-resolved energy (or momentum) distribution curves. The typical energy resolution of the spin-resolved EDCs was 30 meV. The angular step of the spin-resolved MDCs was 0.5° . The polarization of incoming photons was linear horizontal and all measurements were performed at 25 K.

Energy-momentum dispersion around \bar{M}

Fig. 5 (a) presents the linearly dispersing Dirac states along the $\bar{K}\bar{M}\bar{K}$ direction -in the vicinity of \bar{M} - for $\text{Hf}_2\text{Te}_2\text{P}$, $\text{Zr}_2\text{Te}_2\text{P}$, $\text{Ti}_2\text{Te}_2\text{P}$ and $\text{Zr}_2\text{Te}_2\text{As}$. From the MDCs integrated around the Fermi level and the following Lorentzian peak fits shown in Fig. 5 (b), we can distinguish the Fermi momenta of these topological surface states from those of the bulk conduction bands. This is clear experimental proof that the topological states at \bar{M} are metallic. From the EDCs integrated around \bar{M} and the corresponding Lorentzian peak fits shown in Fig. 5 (c), the binding energies E_D of the Dirac points (DPs) and the bulk band-gaps E_{gap} can be extracted. The obtained values are listed in Tab. I.

At \bar{M} , the spin-orbit interaction opens a gap at the crossing point of the parent bulk bands that are mainly composed of Te p -bands, and drives a band inversion inducing a topological surface state in the gap opening. Along the $\bar{\Gamma}\bar{M}\bar{\Gamma}$ direction, these bulk Te p -bands connect with the bulk bands in the vicinity of $\bar{\Gamma}$ (Fig. 6). The image sequence in the bottom panels of Fig. 6 can also track the variations in the size of the energy gap and the energy position of the Dirac point as it will be explained in the

	$\text{Hf}_2\text{Te}_2\text{P}$	$\text{Zr}_2\text{Te}_2\text{P}$	$\text{Ti}_2\text{Te}_2\text{P}$	$\text{Zr}_2\text{Te}_2\text{As}$
$E_D \pm 0.01$ (eV)	1.14	1.01	0.85	1.14
$E_{gap} \pm 0.01$ (eV)	0.48	0.45	0.31	0.43

Table I. Typical quantities characterizing the electronic structures of $\text{M}_2\text{Te}_2\text{X}$ (with $\text{M} = \text{Ti}, \text{Zr}$ or Hf , and $\text{X} = \text{P}$ or As), extracted from the MDCs and EDCs quantitative analysis. E_D s are the binding energies of the Dirac points at \bar{M} . E_{gap} s are the bulk bandgaps at \bar{M} .

next subsection. The values summarized in Tab. I can be related with variations in the strength of the atomic spin-orbit coupling (SOC) among the compounds of the tetradymite family $\text{M}_2\text{Te}_2\text{X}$ (with $\text{M}=\text{Ti}, \text{Zr}$ or Hf and $\text{X}=\text{P}$ or As). SOC is systematically increased by replacing Ti with Zr and finally with Hf, as well as P with As. We may therefore conclude that such an increase of the atomic SOC by elemental substitution is reflected into an increase in E_{gap} (except for the replacement $\text{P}\rightarrow\text{As}$, which keeps the gap essentially unaltered), and E_D . The increase in E_D might be also related to a slight doping caused by defects.

Dirac-Node arcs

Fig. 6 (a-d) present the constant energy maps of $\text{Hf}_2\text{Te}_2\text{P}$, $\text{Zr}_2\text{Te}_2\text{P}$, $\text{Ti}_2\text{Te}_2\text{P}$ and $\text{Zr}_2\text{Te}_2\text{As}$, at binding energies 1.14 eV, 1.00 eV, 0.85 eV and 1.15 eV respectively. These energy values correspond to the energy position of the Dirac point in each different compound. The energy contours show the presence of Dirac-node arcs. Fig. 6 (e-h) show the corresponding energy-momentum dispersion along the Dirac-node arcs, i.e. $\bar{\Gamma}\bar{M}$ direction. The dashed red arrows indicate the binding energies of the Dirac crossing points at \bar{M} . The pointed band bottoms, corresponding to the Dirac-node arcs, are relatively flat, i.e. massive. We note again that, from Hf, to Zr, and to Ti, the strength of spin-orbit coupling (SOC) is systematically reduced. As a direct result, the binding energies of the Dirac point decrease. The binding energy of the Dirac point at \bar{M} in $\text{Zr}_2\text{Te}_2\text{As}$, whose SOC strength is larger than $\text{Zr}_2\text{Te}_2\text{P}$, behaves consistently with the aforementioned observation.

Out-of-plane spin polarisation and total amplitude of the spin polarisation

Fig. 7 presents the out-of-plane component of the spin polarization along the Dirac-node arc of $\text{Ti}_2\text{Te}_2\text{P}$, measured in the same way as Fig. 3 in the main text. As required by symmetry, at \bar{M} , the out-of-plane component of the spin polarization is, within experimental accuracy, zero -see Fig. 7(e). However, as seen in Figs. 7(d, f), a

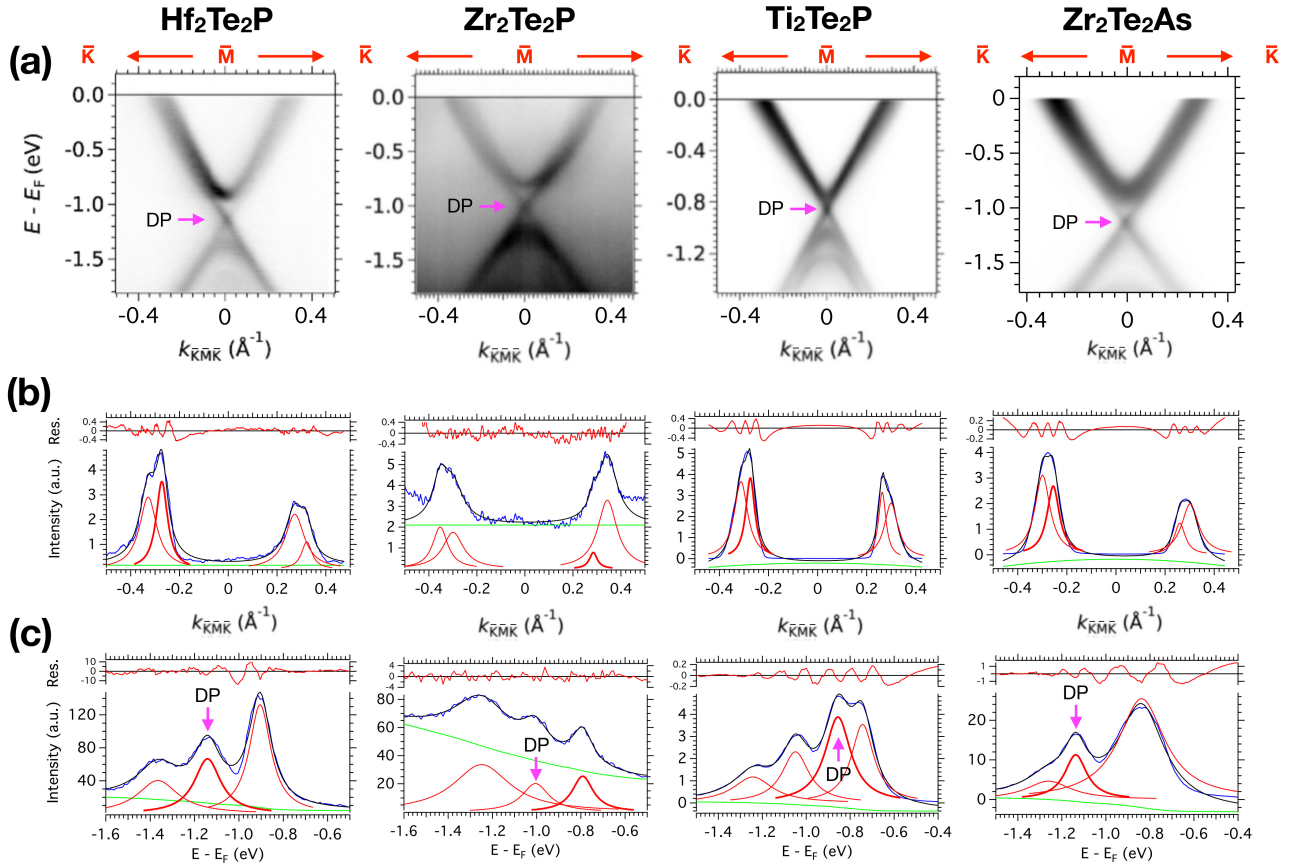


Figure 5. (a) Energy-momentum dispersion along $\bar{K}\bar{M}\bar{K}$ in Hf₂Te₂P, Zr₂Te₂P, Ti₂Te₂P and Zr₂Te₂As. The purple arrows point to the Dirac points (DPs) of linearly dispersing topological surface states. (b) Momentum distribution curves (MDCs) at E_F (integrated over ± 10 meV) of states around \bar{M} in panel (a). (c) Energy distribution curves (EDCs) at \bar{M} (integrated over ± 0.005 \AA^{-1}). These MDCs and EDCs (blue curves) are fitted with Lorentzian peaks (red peaks) and a quadratic (MDC) or Shirley (EDC) background (the green curve). The overall fits are the black curves, while the red line in each top inset is the fitting residual.

small (non-zero) negative out-of-plane spin polarization can be observed away from the \bar{M} point, but still on the Dirac-node arc, for the states comprising its upper and lower cones.

The observed value of the in-plane spin polarization, as shown in the main text, is smaller than 1. The magnitude of the total 3D spin polarization vector would be also below unity, even if we take into account its even smaller out-of-plane projection (Fig. 7) -which, as required by symmetry, vanishes at the \bar{M} point within experimental accuracy. The experimental observation of spin-polarized electrons that are less than 100% polarized is, in fact, not surprising. Similar values of incomplete spin polarization have been previously measured on Bi-based topological insulators [32], thin films and single crystals of Sb and Bi [39–41] and Rashba systems with giant splitting [42, 43]. According to those works, reduced values of spin polarization can be due to the overlap of adjacent photoemission peaks with opposite polarization [32, 39, 42] and/or because of the immediate vicinity of the surface states

with non-polarized bulk bands [40, 41, 43]. Indeed, for all M_2Te_2X compounds the upper branch of the Dirac cone at \bar{M} lies very close to the projected bulk bands that form the petal contours at the Fermi surface, while its lower branch lies close to multiple hole-like states of bulk or surface origin [28]. Moreover, we point out the fact that spin polarization of the photoelectrons in an ARPES experiment can be strongly influenced by the, experimental geometry, photon polarization and photon energy [44–46]. In addition, the limited energy and angular resolution of the experiment would cause the reduction of observed spin-polarization. As a consequence, the exact magnitude of the inherent spin polarization cannot be determined accurately.

Tuning the Dirac points by potassium deposition on the sample's surface

For real applications, it would be desirable to have the Dirac point at E_F such that the backscattering in the

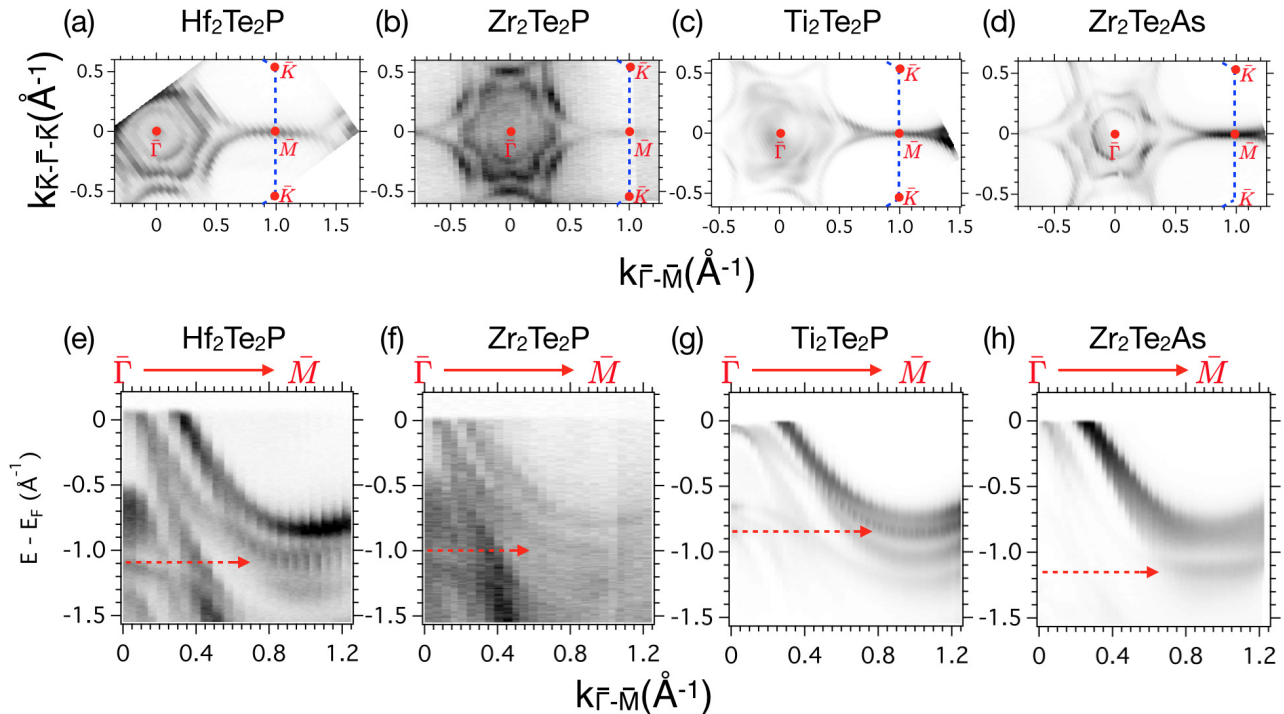


Figure 6. (a-d) Constant energy maps around the Dirac point of $\text{Hf}_2\text{Te}_2\text{P}$, $\text{Zr}_2\text{Te}_2\text{P}$, $\text{Ti}_2\text{Te}_2\text{P}$ and $\text{Zr}_2\text{Te}_2\text{As}$ (hence at binding energies 1.14 eV, 1.00 eV, 0.85 eV and 1.15 eV, respectively), together with the reduced 2D first Brillouin zones (blue dashed lines). (e-h) The electronic dispersions along $\bar{\Gamma}\bar{M}$. The red arrows indicate the quasi-flat states leading to the corresponding Dirac-node arcs. All the data were acquired with LH polarized photons at temperatures $T = 25$ K (a, b, e, f) and $T = 6$ K (c, d, g, h).

solid will be strongly suppressed, leading to dissipationless transport. Note that, according to the DFT calculations, $\text{Hf}_2\text{Te}_2\text{P}$ has an additional Dirac surface state around 200 meV above the Fermi level at $\bar{\Gamma}$ [28, 29], which could even be around 100 meV lower in energy given the observed energy shift between the ARPES data and the calculations. These considerations motivated us to try to tune the Fermi level by potassium (K) deposition at the sample's surface, thus hoping to bring the Dirac point of $\text{Hf}_2\text{Te}_2\text{P}$ within the energy range of the occupied bands. The potassium deposition could also serve to experimentally distinguish the surface states from the bulk states.

Fig. 8(a) shows the electronic states at $\bar{\Gamma}$ along $\bar{K} - \bar{\Gamma} - \bar{K}$ measured at the surface of $\text{Hf}_2\text{Te}_2\text{P}$ capped with 2 Å of potassium. Compared to the bare surface of $\text{Hf}_2\text{Te}_2\text{P}$ in Fig. 8(c), a new hole-like surface state with its top energy right below the Fermi level, indicated with an arrow, appears around $\bar{\Gamma}$. On the other hand, there are no observable energy shifts of the bulk bands except that the signal-to-noise ratio is much lower due to K capping.

Fig. 8(b) shows the electronic states including the Dirac surface state at \bar{M} along $\bar{K} - \bar{M} - \bar{K}$ measured after the K capping at $\text{Hf}_2\text{Te}_2\text{P}$ surface. Compared to Fig. 8(d), the Dirac crossing point of the surface state (SS) is shifted down by around 200 meV to a binding energy 1.35 eV, while the bulk bands (above and below

the gap) remain unchanged.

The fact that surface electron doping (K deposition) shifts only the Dirac cones is an important observation that proves the surface nature of such topological states.

Orbital contribution and band connectivity analysis based on slab DFT calculations

We performed slab DFT calculations of all members of the $\text{M}_2\text{Te}_2\text{X}$ family and found that there is no significant differences in the orbital character of the surface Dirac cones formed at the \bar{M} point between the strong and the weak topological metal members of the family.

In Fig. 9 and 10, we present the results of slab DFT calculations in order to compare the orbital contributions to the Dirac states in the tetradymite compounds with strong (i.e. $\text{Zr}_2\text{Te}_2\text{P}$ and $\text{Ti}_2\text{Te}_2\text{P}$) and weak (i.e. $\text{Hf}_2\text{Te}_2\text{P}$) topological character. In all panels, it is evident that both p (Te) and d (Zr, Hf or Ti) orbitals contribute to the gapless surface state at the \bar{M} point, which may explain the strong anisotropy of the surface states at \bar{M} , in line with the case of Ru_2Sn_3 [33]. The corresponding percentage right at the \bar{M} point is of the order of 60 to 70% for both $\text{Zr}_2\text{Te}_2\text{P}$ and $\text{Hf}_2\text{Te}_2\text{P}$ and stays relatively constant for the upper part of the Dirac cone as

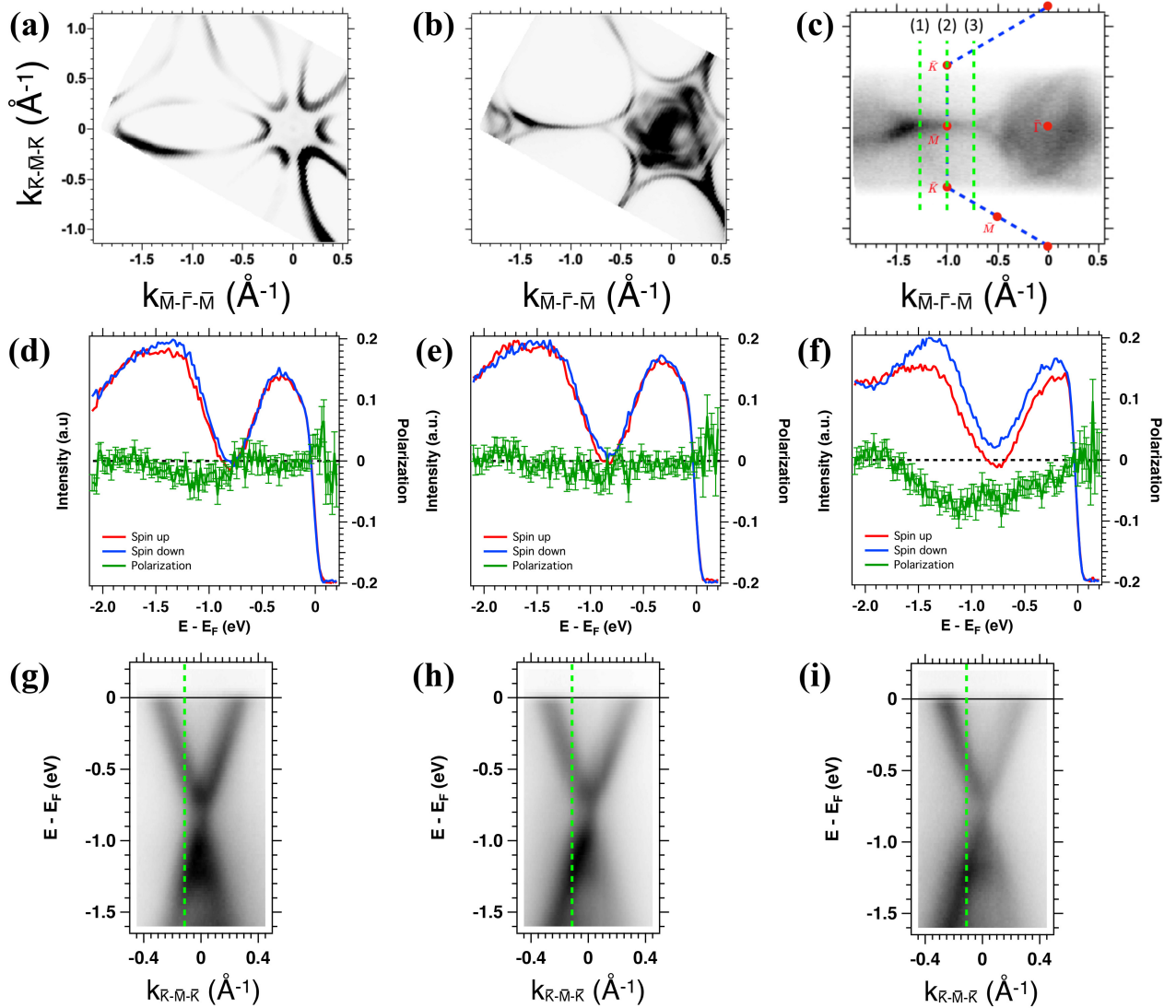


Figure 7. **Out-of-plane spin polarization along the Dirac node arc of $\text{Ti}_2\text{Te}_2\text{P}$.** (a), (b) Spin-integrated ARPES results obtained at synchrotron SOLEIL with LH polarized photons of 50 eV at a temperature of 5 K showing the Fermi surface contours of $\text{Ti}_2\text{Te}_2\text{P}$ (a) and the existence of linear features at a binding energy of 0.85 eV (b). (c) Same as panel (b) but measured with LH photons of 55 eV at the spin-resolved ARPES setup of beamline 9B at HiSOR. Path (1) corresponds to data shown in panels (d) and (g), path (2) to panels (e) and (f), and path (3) to panels (f) and (i). (d)-(f) Spin-resolved EDCs (red, blue) and energy dependent out-of-plane spin polarization along $\bar{\Gamma}\bar{M}$ (green) measured at the left branch of the Dirac cones [panels (g)-(i)], themselves obtained at different k -locations along the Dirac node arc. (g)-(i) Energy-momentum dispersion along the k -paths indicated in panel (c), with overlaid vertical dashed lines showing the k -location of the spin-resolved EDCs shown in panels (d)-(f). Panels (c)-(f) were all measured with LH photons of 55 eV at a temperature of 25 K.

one moves towards \bar{K} . On the other hand, the lower part of the Dirac cone changes progressively to a predominant Zr (or Hf) d character as one approaches \bar{K} . Most importantly, only minor differences in the orbital composition are observed between weak and strong topological metals showing that orbital composition cannot be the key to the different topological character of these compounds.

Our slab calculations in Fig. 11 reveal the detailed dispersion and the connectivity of the electron bands for

both a strong (i.e. $\text{Zr}_2\text{Te}_2\text{P}$) and a weak (i.e. $\text{Hf}_2\text{Te}_2\text{P}$) topological metal member of the $\text{M}_2\text{Te}_2\text{X}$ family. These calculations are in excellent agreement with the massive (almost flat) dispersion of the Dirac-node arc from \bar{M} to $\bar{\Gamma}$. Furthermore, they -once more- confirm $\text{Zr}_2\text{Te}_2\text{P}$ ($\text{Hf}_2\text{Te}_2\text{P}$) as a strong (weak) topological metal by predicting the absence (existence) of a gapless state at $\bar{\Gamma}$ right above the Fermi level. Notice that for the Zr-compound, Fig. 11(a), there is only one Dirac cone at

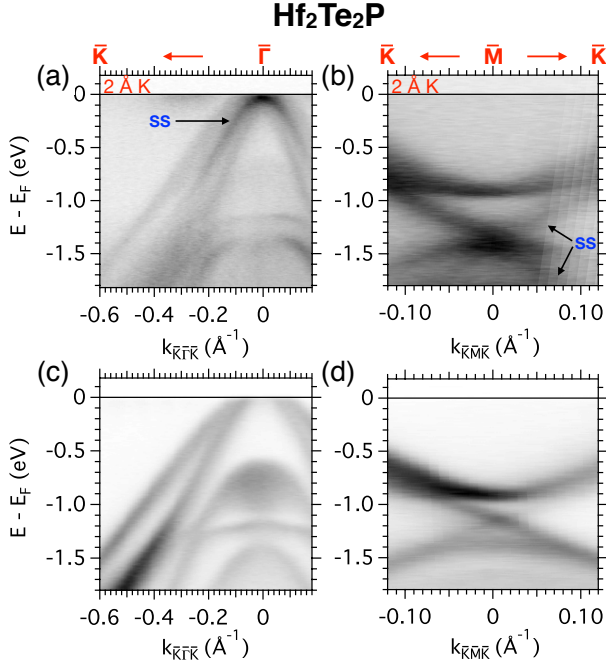


Figure 8. (a, b) ARPES energy-momentum intensity maps at the surface of $\text{Hf}_2\text{Te}_2\text{P}$ capped with 2 Å of potassium, measured respectively at $\bar{\Gamma}$ along $\bar{K} - \bar{\Gamma} - \bar{K}$ and at \bar{M} along $\bar{K} - \bar{M} - \bar{K}$. (c, d) Analogous measurements at the bare (i.e., non capped) surface of $\text{Hf}_2\text{Te}_2\text{P}$. All the data were acquired with LH polarised photons at an energy $h\nu = 50$ eV at $T = 20$ K. The surface state (SS) is indicated by the black arrows in panel (b).

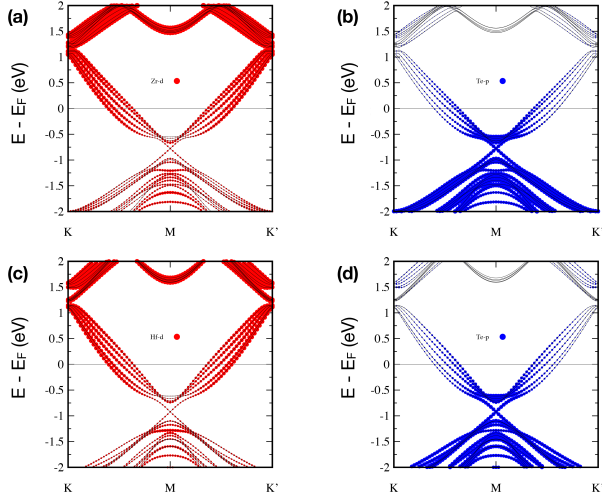


Figure 9. Slab band dispersion along $\bar{K} - \bar{M} - \bar{K}$ high symmetry direction along with the orbital character of the bands: (a, b) Zr- d and Te- p orbital resolved bands for $\text{Zr}_2\text{Te}_2\text{P}$; (c, d) Hf- d and Te- p orbital resolved bands for $\text{Hf}_2\text{Te}_2\text{P}$. The size of the dots is proportional to the percentage of the orbitals mentioned in the figure.

around 0.4 eV, while for the Hf-compound, Fig. 11(c),

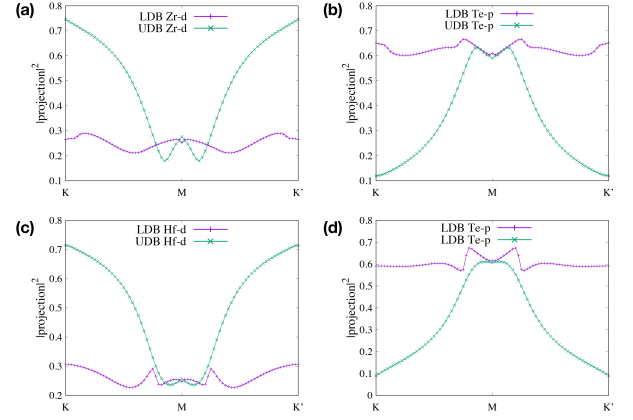


Figure 10. Quantitative comparison of the orbital composition of the bands contributing to the surface Dirac cone state at \bar{M} point: (a, b) $\text{Zr}_2\text{Te}_2\text{P}$; (c, d) $\text{Hf}_2\text{Te}_2\text{P}$. LDB: lower Dirac branch; UDB: upper Dirac branch.

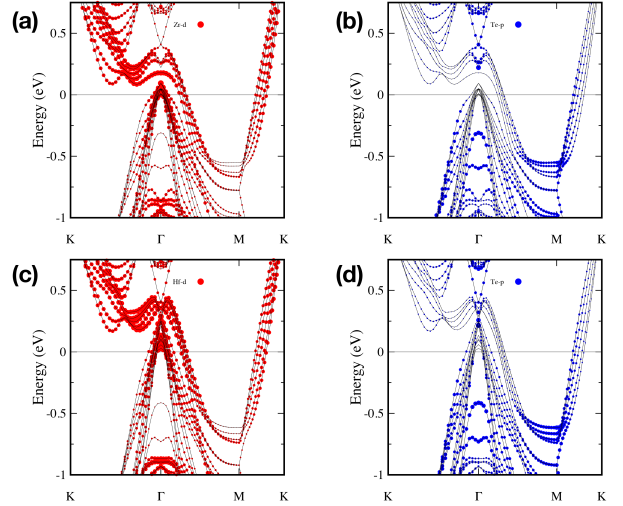


Figure 11. Orbitally resolved slab band dispersion along $\bar{K} - \bar{\Gamma} - \bar{M} - \bar{K}$ direction for (a, b) $\text{Zr}_2\text{Te}_2\text{P}$ and (c, d) $\text{Hf}_2\text{Te}_2\text{P}$.

there are two Dirac cones, one at around 0.4 eV and the other at around 0.25 eV. Notice also that for $\text{Hf}_2\text{Te}_2\text{P}$ the Dirac-node arc does indeed connect with the gapless state at $\bar{\Gamma}$. However, the band connectivity is rather complicated as the surface bands of predominant d character in the Hf-compound cross an even number of times, while in the Zr-compound they cross an odd number of times. Most importantly, the absence of a gapless state at $\bar{\Gamma}$ does not affect the presence of the Dirac-node arc.

* ji.dai@epfl.ch; Present affiliation: Institute of Physics and Lausanne Centre for Ultrafast Science (LACUS), École Polytechnique Fédérale de Lausanne, CH-1015

Lausanne, Switzerland

[†] emmanouil.frantzeskakis@u-psud.fr

[‡] Present affiliation: Condensed Matter Physics and Materials Science Division, Brookhaven National Laboratory, Upton, New York 11973, USA

[§] Present affiliation: Department of Physics, University of Michigan, Ann Arbor, MI, USA

[¶] andres.santander-syro@u-psud.fr

- [1] C. L. Kane and E. J. Mele, Z_2 topological order and the quantum spin hall effect, *Phys. Rev. Lett.* **95**, 146802 (2005).
- [2] M. König, S. Wiedmann, C. Brüne, A. Roth, H. Buhmann, L. W. Molenkamp, X.-L. Qi, and S.-C. Zhang, Quantum spin hall insulator state in hgte quantum wells, *Science* **318**, 766 (2007).
- [3] M. Z. Hasan and C. L. Kane, Colloquium: Topological insulators, *Rev. Mod. Phys.* **82**, 3045 (2010).
- [4] L. Fu, C. L. Kane, and E. J. Mele, Topological insulators in three dimensions, *Phys. Rev. Lett.* **98**, 106803 (2007).
- [5] X.-L. Qi and S.-C. Zhang, Topological insulators and superconductors, *Rev. Mod. Phys.* **83**, 1057 (2011).
- [6] L. Fu, Topological crystalline insulators, *Phys. Rev. Lett.* **106**, 106802 (2011).
- [7] A. A. Soluyanov, D. Gresch, Z. Wang, Q. Wu, M. Troyer, X. Dai, and B. A. Bernevig, Type-II Weyl semimetals, *Nature* **527**, 495 (2015).
- [8] Z. K. Liu, B. Zhou, Y. Zhang, Z. J. Wang, H. M. Weng, D. Prabhakaran, S.-K. Mo, Z. X. Shen, Z. Fang, X. Dai, Z. Hussain, and Y. L. Chen, Discovery of a three-dimensional topological dirac semimetal, na_3bi , *Science* **343**, 864 (2014).
- [9] S.-Y. Xu, C. Liu, S. K. Kushwaha, R. Sankar, J. W. Krizan, I. Belopolski, M. Neupane, G. Bian, N. Alidoust, T.-R. Chang, H.-T. Jeng, C.-Y. Huang, W.-F. Tsai, H. Lin, P. P. Shibayev, F.-C. Chou, R. J. Cava, and M. Z. Hasan, Observation of fermi arc surface states in a topological metal, *Science* **347**, 294 (2015).
- [10] S.-Y. Xu, I. Belopolski, N. Alidoust, M. Neupane, G. Bian, C. Zhang, R. Sankar, G. Chang, Z. Yuan, C.-C. Lee, S.-M. Huang, H. Zheng, J. Ma, D. S. Sanchez, B. Wang, A. Bansil, F. Chou, P. P. Shibayev, H. Lin, and M. Z. Hasan, Discovery of a weyl fermion semimetal and topological fermi arcs, *Science* **349**, 613 (2015).
- [11] A. Stern and N. H. Lindner, Topological quantum computation—from basic concepts to first experiments, *Science* **339**, 1179 (2013).
- [12] V. Lahtinen and J. K. Pachos, A Short Introduction to Topological Quantum Computation, *SciPost Phys.* **3**, 10.21468/SciPostPhys.3.3.021 (2017).
- [13] D. Pesin and A. H. MacDonald, Spintronics and pseudospintronics in graphene and topological insulators, *Nat. Mater.* **11**, 409 (2012).
- [14] N. H. D. Khang, Y. Ueda, and P. N. Hai, A conductive topological insulator with large spin Hall effect for ultralow power spin-orbit torque switching, *Nat. Mater.* **17**, 808 (2018).
- [15] Z. Yue, B. Cai, L. Wang, X. Wang, and M. Gu, Intrinsically core-shell plasmonic dielectric nanostructures with ultrahigh refractive index, *Sci. Adv.* **2**, e1501536 (2016).
- [16] Y. Wu, L.-L. Wang, E. Mun, D. D. Johnson, D. Mou, L. Huang, Y. Lee, S. L. Bud'ko, P. C. Canfield, and A. Kaminski, Dirac node arcs in $PtSn_4$, *Nature Phys.* **12**, 667 (2016).
- [17] D. Takane, Z. Wang, S. Souma, K. Nakayama, C. X. Trang, T. Sato, T. Takahashi, and Y. Ando, Dirac-node arc in the topological line-node semimetal $HfSiS$, *Phys. Rev. B* **94**, 121108 (2016).
- [18] I. Knez, R.-R. Du, and G. Sullivan, Evidence for helical edge modes in inverted $InAs/GaSb$ quantum wells, *Phys. Rev. Lett.* **107**, 136603 (2011).
- [19] Y. Xia, D. Qian, D. Hsieh, L. Wray, A. Pal, H. Lin, A. Bansil, D. Grauer, Y. S. Hor, R. J. Cava, and M. Z. Hasan, *Nat. Phys.* **5**, 398 (2009).
- [20] Y. L. Chen, J. G. Analytis, J.-H. Chu, Z. K. Liu, S.-K. Mo, X. L. Qi, H. J. Zhang, D. H. Lu, X. Dai, Z. Fang, S. C. Zhang, I. R. Fisher, Z. Hussain, and Z.-X. Shen, *Science* **325**, 178 (2009).
- [21] R. Noguchi, T. Takahashi, K. Kuroda, M. Ochi, T. Shira-sawa, M. Sakano, C. Bareille, M. Nakayama, M. D. Watson, K. Yaji, A. Harasawa, H. Iwasawa, P. Dudin, T. K. Kim, M. Hoesch, V. Kandyba, A. Giampetri, A. Barinov, S. Shin, R. Arita, T. Sasagawa, and T. Kondo, A weak topological insulator state in quasi-one-dimensional bismuth iodide, *Nature* **566**, 518 (2019).
- [22] M. Neupane, S.-Y. Xu, R. Sankar, N. Alidoust, G. Bian, C. Liu, I. Belopolski, T.-R. Chang, H.-T. Jeng, H. Lin, A. Bansil, F. Chou, and M. Z. Hasan, Observation of a three-dimensional topological dirac semimetal phase in high-mobility cd_3as_2 , *Nat. Commun.* **5**, 10.1038/ncomms4786 (2014).
- [23] A. A. Burkov, M. D. Hook, and L. Balents, Topological nodal semimetals, *Phys. Rev. B* **84**, 235126 (2011).
- [24] G. Bian, T.-R. Chang, R. Sankar, S.-Y. Xu, H. Zheng, T. Neupert, C.-K. Chiu, S.-M. Huang, G. Chang, I. Belopolski, D. S. Sanchez, M. Neupane, N. Alidoust, C. Liu, B. Wang, C.-C. Lee, H.-T. Jeng, C. Zhang, Z. Yuan, S. Jia, A. Bansil, F. Chou, H. Lin, and M. Z. Hasan, Topological nodal-line fermions in spin-orbit metal $PbTaSe_2$, *Nat. Commun.* **7**, 10.1038/ncomms10556 (2016).
- [25] L. M. Schoop, M. N. Ali, C. Strasser, A. Topp, A. Varykhalov, D. Marchenko, V. Duppel, S. S. P. Parkin, B. V. Lotsch, and C. R. Ast, Dirac cone protected by non-symmorphic symmetry and three-dimensional Dirac line node in $ZrSiS$, *Nat. Commun.* **7**, 10.1038/ncomms11696 (2016).
- [26] K.-W. Chen, S. Das, D. Rhodes, S. Memaran, T. Besara, T. Siegrist, E. Manousakis, L. Balicas, and R. E. Baumbach, Uncovering the behavior of Hf_2Te_2P and the candidate Dirac metal Zr_2Te_2P , *J. Phys.: Condens. Matter* **28**, 14LT01 (2016).
- [27] H. Ji, I. Pletikosić, Q. Gibson, G. Sahasrabudhe, T. Valla, and R. Cava, Strong topological metal material with multiple Dirac cones, *Phys. Rev. B* **93**, 045315 (2016).
- [28] K.-W. Chen, N. Aryal, J. Dai, D. Graf, S. Zhang, S. Das, P. Le Fèvre, F. Bertran, R. Yukawa, K. Horiba, *et al.*, Converting topological insulators into topological metals within the tetradymite family, *Phys. Rev. B* **97**, 165112 (2018).
- [29] M. M. Hosen, K. Dimitri, A. K. Nandy, A. Aperis, R. Sankar, G. Dhakal, P. Maldonado, F. Kabir, C. Sims, F. Chou, D. Kaczorowski, T. Durakiewicz, P. M. Oppeneer, and M. Neupane, Distinct multiple fermionic states in a single topological metal, *Nat. Commun.* **9**, 3002 (2018).
- [30] C. Chen, X. Xu, J. Jiang, S.-C. Wu, Y. P. Qi, L. X. Yang, M. X. Wang, Y. Sun, N. B. M. Schröter, H. F. Yang, L. M. Schoop, Y. Y. Lv, J. Zhou, Y. B. Chen, S. H. Yao,

- M. H. Lu, Y. F. Chen, C. Felser, B. H. Yan, Z. K. Liu, and Y. L. Chen, Dirac line nodes and effect of spin-orbit coupling in the nonsymmorphic critical semimetals $MSiS$ ($M = \text{Hf}, \text{Zr}$), *Phys. Rev. B* **95**, 125126 (2017).
- [31] T. Okuda, K. Miyamaoto, H. Miyahara, K. Kuroda, A. Kimura, H. Namatame, and M. Taniguchi, Efficient spin resolved spectroscopy observation machine at hiroshima synchrotron radiation center, *Rev. Sci. Instr.* **82**, 103302 (2011).
- [32] D. Hsieh, Y. Xia, D. Qian, L. Wray, J. H. Dil, F. Meier, J. Osterwalder, L. Patthey, J. G. Checkelsky, N. P. Ong, A. V. Fedorov, H. Lin, A. Bansil, D. Grauer, Y. S. Hor, R. J. Cava, and M. Z. Hasan, A tunable topological insulator in the spin helical Dirac transport regime, *Nature* **460**, 1101 (2009).
- [33] Q. D. Gibson, D. Evtushinsky, A. Yaresko, V. B. Zabolotnyy, M. N. Ali, M. K. Fuccillo, J. Van den Brink, B. Büchner, R. J. Cava, and S. V. Borisenko, Quasi one dimensional dirac electrons on the surface of Ru_2Sn_3 , *Scientific reports* **4**, 5168 (2014).
- [34] J. Sánchez-Barriga, A. Varykhalov, J. Braun, S.-Y. Xu, N. Alidoust, O. Kornilov, J. Minár, K. Hummer, G. Springholz, G. Bauer, R. Schumann, L. V. Yashina, H. Ebert, M. Z. Hasan, and O. Rader, Photoemission of Bi_2Se_3 with circularly polarized light: Probe of spin polarization or means for spin manipulation?, *Phys. Rev. X* **4**, 011046 (2014).
- [35] P. D. C. King, R. C. Hatch, M. Bianchi, R. Ovsyannikov, C. Lupulescu, G. Landolt, B. Slomski, J. H. Dil, D. Guan, J. L. Mi, E. D. L. Rienks, J. Fink, A. Lindblad, S. Svensson, S. Bao, G. Balakrishnan, B. B. Iversen, J. Osterwalder, W. Eberhardt, F. Baumberger, and P. Hofmann, Large Tunable Rashba Spin Splitting of a Two-Dimensional Electron Gas in Bi_2Se_3 , *Phys. Rev. Lett.* **107**, 096802 (2011).
- [36] M. S. Bahramy, P. D. C. King, A. de la Torre, J. Chang, M. Shi, L. Patthey, G. Balakrishnan, P. Hofmann, R. Arita, N. Nagaosa, and F. Baumberger, *Nat. Commun.* **3**, 1159 (2012).
- [37] T. Okuda, Y. Takeichi, Y. Maeda, A. Harasawa, I. Matsuda, T. Kinoshita, and A. Kakizaki, A new spin-polarized photoemission spectrometer with very high efficiency and energy resolution, *Rev. Sci. Instr.* **79**, 123117 (2008).
- [38] These are not the absolute, but rather relative intensities with arbitrary units since the electron reflectivity of the Fe plate is not taken into account.
- [39] D. Hsieh, L. Wray, D. Qian, Y. Xia, J. H. Dil, F. Meier, L. Patthey, J. Osterwalder, G. Bihlmayer, Y. S. Hor, R. J. Cava, and M. Z. Hasan, Direct observation of spin-polarized surface states in the parent compound of a topological insulator using spin- and angle-resolved photoemission spectroscopy in a mott-polarimetry mode, *New J. Phys.* **12**, 125001 (2010).
- [40] A. Takayama, T. Sato, S. Souma, and T. Takahashi, Rashba effect in antimony and bismuth studied by spin-resolved ARPES, *New J. Phys.* **16**, 055004 (2014).
- [41] T. Hirahara, K. Miyamoto, I. Matsuda, T. Kadono, A. Kimura, T. Nagao, G. Bihlmayer, E. V. Chulkov, S. Qiao, K. Shimada, H. Namatame, M. Taniguchi, and S. Hasegawa, Direct observation of spin splitting in bismuth surface states, *Phys. Rev. B* **76**, 153305 (2007).
- [42] F. Meier, H. Dil, J. Lobo-Checa, L. Patthey, and J. Osterwalder, Quantitative vectorial spin analysis in angle-resolved photoemission: $\text{Bi}/\text{Ag}(111)$ and $\text{Pb}/\text{Ag}(111)$, *Phys. Rev. B* **77**, 165431 (2008).
- [43] K. Yaji, Y. Ohtsubo, S. Hatta, H. Okuyama, K. Miyamoto, T. Okuda, A. Kimura, H. Namatame, M. Taniguchi, and T. Aruga, *Nat. Commun.* **1**, 17 (2010).
- [44] C. Jozwiak, Y. L. Chen, A. V. Fedorov, J. G. Analytis, C. R. Rotundu, A. K. Schmid, J. D. Denlinger, Y.-D. Chuang, D.-H. Lee, I. R. Fisher, R. J. Birgeneau, Z.-X. Shen, Z. Hussain, and A. Lanzara, Widespread spin polarization effects in photoemission from topological insulators, *Phys. Rev. B* **84**, 165113 (2011).
- [45] C. Jozwiak, C.-H. Park, K. Gotlieb, C. Hwang, D.-H. Lee, S. G. Louie, J. D. Denlinger, C. R. Rotundu, R. J. Birgeneau, Z. Hussain, and A. Lanzara, Photoelectron spin-flipping and texture manipulation in a topological insulator, *Nat. Phys.* **9**, 293 (2013).
- [46] J. Sánchez-Barriga, A. Varykhalov, J. Braun, S.-Y. Xu, N. Alidoust, O. Kornilov, J. Minár, K. Hummer, G. Springholz, G. Bauer, R. Schumann, L. V. Yashina, H. Ebert, M. Z. Hasan, and O. Rader, Photoemission of Bi_2Se_3 with Circularly Polarized Light: Probe of Spin Polarization or Means for Spin Manipulation?, *Phys. Rev. X* **4**, 011046 (2014).